

Water Maser Kinematics in the Jet of OH 12.8–0.9

David A. Boboltz

*U.S. Naval Observatory,
3450 Massachusetts Ave., NW, Washington, DC 20392-5420,
dboboltz@usno.navy.mil*

and

Kevin B. Marvel

*American Astronomical Society,
2000 Florida Ave., NW, Suite 400, Washington, D.C., 20009-1231,
marvel@aas.org*

ABSTRACT

We present Very Long Baseline Array observations of the kinematics of the water masers associated with OH 12.8–0.9, the fourth member of the so-called “water fountain” class of sources. We find that the masers occupy two distinct regions at the ends of a bipolar jet-like structure oriented north–south, with the blue-shifted masers located to the north and the red-shifted masers to the south. The masers are distributed along arc-like structures 12–20 mas across oriented perpendicular to the separation axis with an angular separation of ~ 110 mas on the sky. Our multi-epoch observations, show the two maser arcs to be expanding away from each other along the axis of separation. The relative proper motions of the two maser regions is 2.7 mas yr^{-1} ($\sim 105 \text{ km s}^{-1}$ at the assumed distance of 8 kpc). The measured radial velocity difference between the northern, blue-shifted masers and the southern, red-shifted masers is 48.4 km s^{-1} . The radial velocity, when combined with the proper motion, yields a three-dimensional expansion velocity of 58 km s^{-1} and an inclination angle of 24° for the jet. By combining our radial velocities with historical values, we estimate the three dimensional acceleration of the masers to be $\sim 0.63 \text{ km s}^{-1} \text{ yr}^{-1}$ and a dynamical age for the collimated outflow of $\sim 90 \text{ yr}$.

Subject headings: circumstellar matter — masers — stars: AGB and post AGB — stars: mass-loss — stars: individual (OH 12.8–0.9)

1. INTRODUCTION

In the study of stars and stellar evolution, certain stages in the stellar life cycle remain a mystery simply because of their transitory nature. The evolutionary stage between the end of the asymptotic giant branch (AGB) and the planetary nebula (PN) phase is one such example. As stars evolve up the AGB, they lose mass at an increasing rate and spherically symmetric circumstellar envelopes (CSEs) are formed. Despite the spherical symmetry of the mass-loss process, a large fraction ($\sim 75\%$) of planetary nebulae (PNs) show aspherical (i.e. elliptical, bipolar, quadrupolar) morphologies (Manchado et al. 2000). The shaping of asymmetrical PNs must therefore occur over the relatively short time period of 10^3 – 10^4 yr that the star spends in a post-AGB or proto-planetary nebula (PPN) phase (Kwok 1993). Based on comparative studies of compact and extended PNs, Aaquist & Kwok (1996) find that the lack of difference in the morphologies between the two groups suggests that PNs morphologies are primarily inherited from the AGB evolutionary stage. Sahai & Trauger (1998) surveyed a number of young PNs with the Hubble Space Telescope Wide Field Planetary Camera 2 and found that the majority of them were characterized by multi-polar bubbles distributed in a point-symmetric fashion about the central star. They also found collimated radial structures and bright equatorial structures indicating the presence of jets and disks/torii in some objects. These observations led Sahai & Trauger (1998) to propose a mechanism in which high-speed collimated outflows operate during the late-AGB or early PPN stages of stellar evolution. During this phase, the jet-like outflows carve out an imprint in the spherical AGB wind, and it is this imprint that provides the morphological signature necessary for the development of aspherical PNs.

There is a small number of evolved objects that have been shown to exhibit the types of collimated jet-like outflows described above. These objects, dubbed “water fountain” nebulae, are thought to be stars entering the post-AGB or PPN evolutionary stage. They exhibit both H_2O and OH maser emission, however, the relative characteristics of the two maser species differ from those of the typical AGB star. These differences are apparent in both the spectral profiles of the two types of masers and in the unique spatial morphologies of the masers as measured by radio interferometry. Prior to our study of OH 12.8–0.9 (Boboltz & Marvel 2005), there were three confirmed water-fountain sources: IRAS 16342–3814 (Sahai et al. 1999; Morris et al. 2003), IRAS 19134+2131 (Imai et al. 2004), and W43A (Imai et al. 2002).

Spectrally, these water-fountain sources exhibit double-peaked OH and H_2O maser profiles with the peaks symmetrically distributed about the radial velocity of the star. However, unlike the typical evolved star, the H_2O maser peaks have a greater spread in velocity than the corresponding OH masers. For IRAS 16342–3814, IRAS 19134+2131, and W43A these

velocity ranges for the H₂O masers are 259 km s⁻¹, 132 km s⁻¹ and 180 km s⁻¹ respectively (Likkell et al. 1992). In addition, the expansion velocities (>60 km s⁻¹) implied by the maser spectra are much greater than the expansion velocity for the circumstellar wind of a typical AGB star (5–30 km s⁻¹).

Spatially, the H₂O masers associated with these sources are known to trace bipolar jet-like outflows, hence the "water fountain" name. In the first Very Long Baseline Interferometry (VLBI) study of the H₂O masers toward W43A, Imai et al. (2002) showed that the water masers are formed in a collimated precessing jet with an estimated 3-D outflow velocity of 145 km s⁻¹. Interferometric studies of IRAS 16342–3814 (Morris et al. 2003; Claussen et al. 2004) and IRAS 19134+2131 (Imai et al. 2004) also found the H₂O masers to exhibit bipolar distributions. Three-dimensional outflow velocities for IRAS 16342–3814 and IRAS 19134+2131 are 185 km s⁻¹ and 130 km s⁻¹, respectively. The bipolar jets traced by the H₂O masers, presumably along the polar axis of the star, may represent the onset of the axisymmetric morphologies that typify PNs. The dynamical ages of the jets for IRAS 19134+2131 and W43A are estimated to be ~50 yr and ~40 yr, respectively (Imai et al. 2002, 2004). That for IRAS 16342–3814 is estimated to be ~150 yr (Claussen et al. 2004).

The enigmatic source OH 12.8–0.9 was first classified by Baud et al. (1979) as a Type II OH/IR star based on its characteristic double-peaked 1612-MHz OH maser profile. The distance to the source is unknown although Baud et al. (1985) included it in a sample of OH/IR stars associated with the Galactic center. OH 12.8–0.9 has been linked to the infrared source IRAS 18139–1816, which is ~26 arcsec away (te Lintel Hekkert et al. 1989). The SIMBAD astronomical database, however, still lists two separate entries for the source, one for each identifier. Classification of IRAS 18139–1816 based on IRAS Low Resolution Spectrometer (8–23 μm) data was performed by Kwok et al. (1997) who placed the source in category *I*, a group with noisy or incomplete spectra. Kwok et al. (1997) also noted that IRAS 18139–1816 is a "25 μm peaker", or a source whose IRAS flux density at 25 μm is greater than its flux density at both 12 and 60 μm. Other 25 μm peakers include young planetary nebulae and carbon stars with circumstellar silicate emission features (Kwok et al. 1997). OH 12.8–0.9 has been also observed with the PHT-S (2.5–11.6 μm) spectrophotometer onboard the Infrared Space Observatory (ISO). From the spectra, Hodge et al. (2004) classify the source in the *4/5.SA* category. Sources in the *4/5* group peak long-ward of the 11.6 μm limit of the PHT-S. Objects in the *4/5.SA* sub-group additionally exhibit a deep 10 μm absorption feature and absorption features from H₂O at 3 and 6 μm, CO₂ at ~4.3 μm, and CO at ~4.6 μm (Hodge et al. 2004).

H₂O maser emission from OH 12.8–0.9 was first detected by Engels et al. (1986) who noted the fact that the H₂O emission peaks are outside the range of the OH maser emission.

Gómez et al. (1994) used the Very Large Array (VLA) to show that the “anomalous” H₂O and OH maser emission was spatially coincident to within 1”, and therefore belonged to the same source. Gómez et al. (1994) also found double-peaked profiles for both the OH and the H₂O with the peaks of the OH separated by $\sim 23 \text{ km s}^{-1}$ and H₂O peaks separated by nearly twice this amount, $\sim 42 \text{ km s}^{-1}$. Although the velocity range for the H₂O is not as wide as the other water-fountain sources, Engels (2002) found that the shape and variations in the spectra were consistent with the water-fountain class and compatible with an axisymmetric wind.

In Boboltz & Marvel (2005) we reported on our initial Very Long Baseline Array (VLBA) observations of the H₂O masers associated with OH 12.8–0.9. We found that the H₂O masers trace the bipolar morphology typical of the water-fountain class. This bipolar structure combined with the spectral characteristics of the H₂O and OH maser emission led us to propose that OH 12.8–0.9 is a fourth member of the rare water-fountain class of objects. In this article, we present additional multi-epoch observations made with the VLBA with the goal of measuring the kinematics of the H₂O masers that trace the jet of OH 12.8–0.9.

2. OBSERVATIONS

We observed the 22.2 GHz H₂O maser emission from OH 12.8–0.9 ($\alpha = 18^h 16^m 49^s .23$, $\delta = -18^\circ 15' 01'' .8$, J2000) using the 10 stations of the VLBA. The VLBA is operated by the National Radio Astronomy Observatory (NRAO).¹ VLBA spectral-line observations occurred on 2004 June 21, 2005 July 21, 2005 Nov. 2, and 2006 Feb. 24. Each observing run was approximately 5 hrs in length. A reference frequency of 22.23508 GHz was used for the H₂O maser transition. Data were recorded in dual circular polarization using two 8-MHz (112.6 km s^{-1}) bands centered on the local standard of rest (LSR) velocity of -58.0 km s^{-1} .

For an unknown reason, the observations made on 2005 July 21 did not detect the H₂O masers from OH 12.8–0.9. Following this non-detection, we requested a short (5 minute) observation of OH 12.8–0.9 with the Green Bank Telescope (GBT) in order to decide whether the masers would still be detectable in the pending two epochs of VLBA observations. On 2005 Sept. 13 the GBT observed the H₂O maser spectrum and found masers at levels of 2–3 Jy. We therefore continued with remaining two scheduled VLBA epochs and subsequently managed to detect and image the masers. The remainder of this article relates only to the three epochs in which the maser observations were successful, hereafter denoted: epoch 1

¹The National Radio Astronomy Observatory is a facility of the National Science Foundation operated under cooperative agreement by Associated Universities, Inc.

(2004 June 21), epoch 2 (2005 Nov. 2), and epoch 3 (2006 Feb. 24).

The data were correlated at the VLBA correlator operated by NRAO in Socorro, New Mexico. Auto and cross-correlation spectra consisting of 512 channels with channel spacings of 15.63 kHz ($\sim 0.22 \text{ km s}^{-1}$) were produced by the correlator. Calibration of each of the three epochs was performed in accordance with standard VLBA spectral-line procedures using the Astronomical Image Processing System (AIPS) maintained by NRAO. The calibration of epoch 1 is described in Boboltz & Marvel (2005) and the two subsequent epochs were calibrated in a similar manner. For each epoch, residual delays due to the instrumentation were corrected by performing a fringe fit on the continuum calibrator (J1751+0939) scans. Residual group delays for each antenna were determined and applied to the target data.

The bandpass response was determined from scans on J1751+0939 and was used to correct the OH 12.8–0.9 data. The time-dependent gains of all antennas relative to a reference antenna were determined by fitting a total-power spectrum (from the reference antenna with the target source at a high elevation) to the total power spectrum of each antenna. The absolute flux density scale was established by scaling these gains by the system temperature and gain of the reference antenna. Errors in the gain and pointing of the reference antenna and atmospheric opacity variations contribute to the error in the absolute amplitude calibration, which is accurate to about 15–20%.

Residual fringe rates were obtained by fringe-fitting a strong reference feature in the spectrum of OH 12.8–0.9. For each epoch we used the same strong feature at channel velocity $V_{\text{LSR}} = -81.6 \text{ km s}^{-1}$. The resulting fringe-rate solutions were applied to all channels in the spectrum. An iterative self-calibration and imaging procedure was then performed to map the emission in the reference channel for each epoch. The resulting residual phase and amplitude corrections from the reference channel were then applied to all channels in the 8-MHz band. All of the above calibrations were then applied to the data prior to imaging.

Imaging of the epoch 1 data is discussed in Boboltz & Marvel (2005), and a similar methodology was employed for the two subsequent epochs. For epochs 2 and 3, full resolution images 2048×2048 pixels ($\sim 160 \times 160 \text{ mas}$) were generated using a synthesized beam sizes of $1.08 \times 0.39 \text{ mas}$ for epoch 2 and $0.88 \times 0.33 \text{ mas}$ for epoch 3. Images were produced for all spectral channels from -88.3 km s^{-1} to -25.1 km s^{-1} forming an image cube of 301 image planes. Since peak maser flux densities were on the order of 1 Jy, channel images are noise limited and do not suffer from dynamic range limitations as is often the case in maser observations. Typical 1σ off-source noise estimates for individual image planes were 8–10 mJy beam^{-1} for epoch 2 and 10–12 mJy beam^{-1} for epoch 3. The analysis and extraction of relevant information from the image cubes is described below.

3. RESULTS

In order to identify and extract maser component parameters, two-dimensional Gaussian functions were fit to the emission in the image plane of each spectral (velocity) channel using the AIPS task SAD. Image quality was assessed using the off-source rms noise in the image. A cutoff flux density was set at five times the rms noise in the image plane containing the emission. Emission features with flux densities greater than the cutoff were fit with Gaussians to determine maser component parameters. The errors in right ascension and declination of the Gaussian fits to the identified components were computed by the AIPS task SAD following the method outlined by Condon (1997). These position errors ranged from $5 \mu\text{as}$ for features with high signal-to-noise, to $110 \mu\text{as}$ for features with lower signal-to-noise.

Figures 1 and 2 show the spectral (upper sub-panels) and spatial (lower sub-panels) distributions of the H_2O masers toward OH 12.8–0.9 from the analysis of our VLBA images for epoch 2 (Fig. 1) and epoch 3 (Fig. 2). A similar plot for epoch 1 was presented in Boboltz & Marvel (2005). In the figures, panel (a) shows the entire range of H_2O maser emission from the star. Panels (b) and (c) show enlarged views of the blue-shifted masers to the north and the red-shifted masers to the south, respectively.

In the upper sub-panels in Figures 1(a) and 2(a), the H_2O maser spectra for epochs 2 and 3 are plotted along with the spectrum of the 1612-MHz OH masers from previous observations (Boboltz & Marvel 2005) as a reference. The velocities of the OH maser peaks, have not changed significantly over time when compared to previous observations of Gómez et al. (1994). We observed the velocities of the blue- and red-shifted OH peaks to be -68.0 and -43.7 km s^{-1} , respectively with a velocity resolution of 0.18 km s^{-1} . By comparison, the velocities of the two peaks reported in Gómez et al. (1994) are essentially the same at -67.4 and -44.0 km s^{-1} , to within the velocity resolution of their VLA observations (1.1 km s^{-1}). As in epoch 1, the H_2O masers form a double-peaked profile with a velocity extent greater than that of the double-peaked OH maser profile. On the blue-shifted side of the emission, the peak flux density of epoch 2 remained the same as for epoch 1 at 1.3 Jy beam^{-1} and decreased slightly in epoch 3 to $0.97 \text{ Jy beam}^{-1}$. For the red-shifted emission, the peak flux density steadily decreased from 1.0 Jy beam^{-1} in epoch 1 to 0.6 Jy beam^{-1} in epoch 2 to 0.2 Jy beam^{-1} in epoch 3. The velocity distributions for the masers in epochs 2 and 3 are very similar to those in epoch 1 and will be discussed in detail in § 3.2.

The lower sub-panels of Figures 1(a) and 2(a) show the entire spatial extent of the H_2O masers for epochs 2 and 3, respectively. Enlarged views of the north and south regions are also shown in panels (b) and (c) of each figure. We find that in epochs 2 and 3 the overall spatial structure of the H_2O masers has remained essentially unchanged from epoch 1. There are two distinct regions oriented roughly north–south on the sky separated by

~ 110 mas. The position angle of the axis of separation between the mean position centers of the northern and southern maser regions is $\sim 2.6^\circ$ east of north. The masers in the two regions are arranged in arc-like structures oriented roughly east–west with the exception of the feature located near $(15.0, -10.0)$ in Figures 1(b) and 2(b). This feature, although apparent in the epoch 1 image cube, did not meet all of the component selection criteria in our initial analysis of the data (Boboltz & Marvel 2005). The feature is discussed further in § 3.1 below. The blue- and red-shifted arcs of masers are approximately 20 and 12 mas across, respectively, corresponding opening angles for the jet of 13–20°.

3.1. Maser Proper Motions

In Figures 1 and 2, we plotted the maser emission identified in every spectral channel, thus an individual maser feature will appear in multiple spectral channels and will consist of multiple points in the spatial distributions shown in the figures. In order to track and estimate the motions of the maser features, it is necessary to determine average values in right ascension, declination, and velocity for each feature. These average values were computed using a flux-density-squared weighted average for emission identified in two or more channels and spatially coincident to within 1 mas. The flux assigned to the maser feature was simply the peak flux in the channels spanned by the feature. Characteristics of the masers for the three epochs are presented in Tables 1–3.

Since we did not use the technique of phase-referencing for our three VLBA epochs, the absolute position of the phase center in each image cube is unknown. However, in the reduction and analysis of each epoch of observations, we used what we believe to be the same maser feature as a phase reference. This feature was the strongest feature in each of the three epochs. In addition, it maintained the same velocity and spatial location relative to the other three northern, blue-shifted masers common to all three epochs. The averaging of the maser identifications over several channels resulted in slight (< 0.1 mas) position shifts for the reference feature in each of the three epochs. The coordinate frames for all three epochs were therefore realigned such that the reference feature (the third blue-shifted feature in Tables 1 and the second blue-shifted feature in Tables 2 and 3) coincided with the origin.

Relevant maser characteristics determined from the analysis are plotted in Figures 3 and 4. Figure 3 shows the blue-shifted H_2O masers in the north of OH 12.8–0.9. In this figure, the alignment of the reference features for the three epochs at the origin is apparent. Also common to all three epochs are features near $(-2.0, 0.5)$, $(8.0, 0.2)$ and $(15.0, -10.0)$. As mentioned earlier, the feature near $(15.0, -10.0)$ did not appear in Boboltz & Marvel (2005) because it did not meet all of the selection criteria at the time. However, with the

additional knowledge from epochs 2 and 3, and some reprocessing of the epoch 1 image cube, we were able to extract the relevant parameters for this feature. From Figure 3 it is apparent that any position differences between the three epochs are small, thus indicating little motion of the northern features relative to the reference feature over the course of the three experiments. This, however, is not the case for the southern maser features. Figure 4 shows the red-shifted H₂O masers in the south of OH 12.8–0.9. Here there are five features that are common to all three epochs. Clearly there is a consistent proper motion of all of the features nearly due south relative to the blue-shifted reference feature. The average angular separations of the north and south masers are 107, 110 and 111 mas for epochs 1, 2 and 3, respectively. As discussed in Boboltz & Marvel (2005) the distance to OH 12.8–0.9 is not well known. Best estimates place the object near the Galactic center at $D \approx 8$ kpc (Baud et al. 1985). Assuming this distance, then the linear separations between the blue- and red-shifted masers are approximately 860, 880 and 890 AU, respectively.

In order to better characterize the net expansion of the masers we computed separations between pairwise combinations of components. This technique has previously been used to characterize OH (Chapman et al. 1991; Bloemhof et al. 1992; Kemball 1992), H₂O (Marvel 1996), and SiO (Boboltz et al. 1997; Chen et al. 2006) maser motions and has no dependence on the alignment of the maps or a priori assumptions about the velocity field. The procedure involves computing the angular separation ($\Delta\theta$) between two features at one epoch (epoch A) and the separation between the corresponding two features at a second epoch (epoch B). The difference between the two values of $\Delta\theta$ is the pairwise separation and can be written

$$\Delta\theta_B - \Delta\theta_A = |r_i - r_j|_B - |r_i - r_j|_A, \quad i = 1, n; \quad j = i + 1, n \quad (1)$$

where $r_i = (x_i, y_i)$ and (x_i, y_i) are the relative offsets in right ascension and declination, respectively. The procedure is repeated for all possible pair combinations and the separations can be plotted as a histogram (e.g. Figure 5). The inclusion of all possible pair combinations often results in bimodal distribution with one of the peaks biased towards zero. This is because some of the separations involve pairs of closely spaced maser components on the same side of the distribution (i.e. the northern or southern regions for OH 12.8–0.9) that have little motion relative to one another. For the sake of clarity, and to determine representative values for the angular shifts due to the expansion, we have included only those pairs separated by more than 80 mas in the histograms shown in Figure 5. Figure 5 plots the pairwise separations over time intervals of (a) 613, (b) 500 and (c) 114 days, respectively. All three histograms have centroids which are biased toward positive values indicative of expansion. The mean (median) differences between the north and south masers are 4.64 (4.69) mas, 3.88 (3.89) mas, and 0.77 (0.80) mas for 613, 500, and 114 days, respectively. The 1σ standard deviations are 0.28, 0.21 and 0.13 mas, respectively. The equivalent mean angular velocities are 2.76 ± 0.16 mas yr⁻¹, 2.83 ± 0.15 mas yr⁻¹ and 2.47 ± 0.41 mas yr⁻¹. To within the

errors, the three velocities are consistent, and it is impossible to determine whether there is any acceleration of the masers in the outflow.

If 8 kpc is again assumed as the distance to OH 12.8–0.9, the linear proper motions of the masers can be computed for the angular velocities above. The resulting average linear separation velocities are $105 \pm 6 \text{ km s}^{-1}$, $107 \pm 6 \text{ km s}^{-1}$ and $94 \pm 16 \text{ km s}^{-1}$ for the 613, 500, and 114 day intervals respectively. If we assume that the north and south masers are moving outward at equal speeds (i.e. at half the computed separation velocity), then the outflow velocity in the plane of the sky would be $\sim 53 \text{ km s}^{-1}$ for the 613 day interval. This velocity is slightly more than double the outflow velocity determined for OH 12.8–0.9 in Boboltz & Marvel (2005) based solely on the radial velocities. In the following section we update the radial velocities of the masers and combine them with the proper motions in order to estimate the full 3-D kinematics of the masers in the jet.

3.2. 3-D Maser Outflow

In Boboltz & Marvel (2005), we treated the radial velocity of OH 12.8–0.9 by simply determining the velocity separation of the blue- and red-shifted maser features representing the peaks in the spectral distribution. This was an improvement over previous single-dish and VLA studies that contained limited spatial information and likely suffered from blending of features in the spectral domain. In light of the two new epochs of VLBA data, we felt that the more rigorous approach of computing spectral separations (Δv) from multiple features was more appropriate. To do this we averaged the velocities of the blue- and red-shifted masers identified in Tables 1–3 separately. We also computed the standard deviations for each set of components. From these averages we computed the spectral separation Δv at each epoch. The error in Δv is simply the standard deviations added in quadrature. Using this method, we find mean values for Δv of $48.7 \pm 1.6 \text{ km s}^{-1}$, $48.3 \pm 1.3 \text{ km s}^{-1}$ and $48.2 \pm 1.3 \text{ km s}^{-1}$ for epochs 1, 2, and 3, respectively. These values are also listed in Table 4.

In Boboltz & Marvel (2005) we compared the spectral separation of the blue- and red-shifted peaks in our spectrum with peak separations from previous single dish and VLA observations (i.e. Engels et al. 1986; Gómez et al. 1994; Engels 2002). Here we wish to compare our spectral separations computed from the component averages with these previous results, however, only Engels (2002) tabulates parameters for individual spectral features. Engels (2002) categorizes components A–H of his Table 4 into the blue-shifted group and components M–Q of Table 5 into the red-shifted group, with the remaining components, I–L, listed as intermediate. From this information, we computed average velocities for the blue- and red-shifted spectral features and values for Δv in a manner similar to that performed

for our own VLBA data. The resulting values of Δv and the corresponding errors for the Engels (2002) are listed in Table 4. The only drawback to the Engels data as compared to our VLBA data is the fact that there is no spatial information, thus the degree to which spectral blending is a factor is unknown. It should be noted, that the spectral resolution of the Engels measurements is slightly better than our VLBA resolution at 0.16 km s^{-1} .

Plotted in Figure 6 are the results of our computation of Δv from the blue- and red-shifted component averages. The values from the 11 epochs of Engels (2002) are plotted as filled triangles and those from our three epochs of VLBA data as filled circles. The data clearly shows an increase in Δv as a function of time. To this data, we performed a linear least-squares fit weighted by squares of the errors. This fit is plotted as the line in Figure 6, with a slope of $0.53 \pm 0.04 \text{ km s}^{-1} \text{ yr}^{-1}$ corresponding to the relative acceleration of the blue- and red-shifted masers in the radial direction. This is slightly lower than the $0.68 \pm 0.06 \text{ km s}^{-1} \text{ yr}^{-1}$ reported in Boboltz & Marvel (2005). With the new procedure of averaging over multiple spectral features, we have attempted to remove the error involved in computing the velocity separation from single peaks on the blue- and red-shifted sides of the spectrum that are likely unrelated over over periods greater than the lifetime of the components $< 3 \text{ yr}$ Engels (2002). Engels also discusses $\sim 1 \text{ km s}^{-1}$ velocity shifts that were observed for some components in the spectra of OH12.8–0.9 and the likelihood of these shifts being caused by intensity changes within blended features. Such shifts could affect the velocity separations computed from single spectral peaks as was done in Boboltz & Marvel (2005).

If we assume an average over our three VLBA epochs, $\Delta v \approx 48 \text{ km s}^{-1}$, as the speed the masers are moving away from each other along the line of sight to the observer, then the outflow velocity in the radial direction is $\sim 24 \text{ km s}^{-1}$. The 3-D outflow velocity of the masers may be estimated by combining the radial motion above with the motion in the plane of the sky determined in § 3.1. We find the 3-D outflow velocity of the masers to be $\sim 58 \text{ km s}^{-1}$ with an inclination angle for the jet of $\sim 24^\circ$ with respect to the plane of the sky. The 3-D outflow acceleration, assuming this inclination angle and the radial acceleration above, is $\sim 0.63 \text{ km s}^{-1} \text{ yr}^{-1}$. The outflow acceleration in the plane of the sky would be $\sim 0.58 \text{ km s}^{-1} \text{ yr}^{-1}$ under this assumption. Thus over the 613 days between epochs 1 and 3, we could expect a change in velocity of the blue-shifted masers relative to the red-shifted masers of 1.93 km s^{-1} or 0.05 mas yr^{-1} , which is undetectable in our present observations.

From the above information and two additional assumptions, namely: that the dynamical center of the outflow is the midpoint along the axis of separation between the two maser regions and that the masers have zero initial velocity, then an upper limit to the dynamical age of the outflow can be computed. We find this dynamical age to be $\sim 90 \text{ yr}$. This value

is roughly consistent with the age determined in Boboltz & Marvel (2005), which was estimated with no knowledge of the maser motions in the plane of the sky or the inclination angle of the outflow. Assuming that the acceleration has and will remain constant at the above value of $0.63 \text{ km s}^{-1} \text{ yr}^{-1}$, then the total time to reach an outflow velocity comparable to the other water fountain sources ($\Delta v \approx 150 \text{ km s}^{-1}$) is only about $\sim 240 \text{ yr}$, roughly 2.5 times the current dynamical age of OH 12.8–0.9.

In order to compare the characteristics of OH 12.8–0.9 to the other water-fountain sources, we have summarized the relevant properties of all four sources in Table 5. From the table we see that the assumed distance to OH 12.8–0.9 is intermediate among the four sources. The peak flux density is shown as a range measured over multiple epochs by Engels (2002) for OH 12.8–0.9 and by Likkell et al. (1992) for the three other sources. The peak flux range for OH 12.8–0.9 is similar to that of the other distant source IRAS 19134+2131 and weaker than those of W 43A and IRAS 16342–3814. The angular extent of the outflow on the plane of the sky is also similar to that of IRAS 19134+2131. The linear extent of OH 12.8–0.9, however, is much less than that of any of the other water-fountain sources. An increase in the assumed distance to the source, would serve to bring this value in line with the other sources. For the collimation of the OH 12.8–0.9 jet, we have used an average of the northern and southern arcs and find that the collimation is slightly larger than for the other three water-fountain sources. If we use only the southern arc, or we disregard the one northern feature at (15.0, –10.0) then the collimation is $\sim 10^\circ$, which is consistent with the other water-fountain sources. The estimated inclination angle of the outflow is also comparable values estimated for the other three objects.

Aside from the difference in linear extent, the primary difference between OH 12.8–0.9 and the other water-fountain sources is in the kinematics. Both the radial (v_{rad}) and tangential (v_{tan}) outflow velocities are less than half the values for the other sources. It is possible that the tangential velocity could be closer to that of the other sources if the distance to the source turns out to be greater than 8 kpc. An increased distance would not increase the radial velocity estimate, but would instead result in a decreased estimate for the inclination angle of the jet. Another major difference between OH 12.8–0.9 and the three other water fountains is that OH 12.8–0.9 appears to be the only object with a measurable acceleration (a_{rad}) of the masers along the line of sight. Likkell et al. (1992) observed the H_2O maser spectra of the three other water-fountain sources over the course of a few years and found no evidence for systematic velocity drifts in spectral features that would suggest acceleration of the masers. The acceleration in combination with the smaller extent of the masers toward OH 12.8–0.9 might suggest that it is younger than the other three objects. This is not, however, confirmed by the computed dynamical age of the jet, which is intermediate among the four sources at 90 yr.

One characteristic that is not shown in the tables is the morphology of the masers relative to the central star and the jet direction. From the images of OH 12.8–0.9 presented here, we find that the masers are arranged in point symmetric fashion along arcs perpendicular to the direction of the outflow, suggesting that the outflow is impacting a denser surrounding medium. This bow shock structure is also observed for the H₂O masers toward IRAS 16342–3814 at least for the blue-shifted side of the jet (Claussen et al. 2004). These two sources are in contrast to W 43A where the masers are arranged along the direction of the outflow. The structure of the W 43A masers is well represented by a precessing jet model (Imai et al. 2002, 2005). The remaining water-fountain source, IRAS 19134+2131, shows the point symmetric morphology of the three other sources, but the relationship between the masers and the outflow is less clear. From the two epochs of VLBI observations reported in Imai et al. (2004), the masers on the eastern red-shifted side appear to be roughly aligned with the line connecting them to the western blue-shifted masers. The motions of the masers, however, do not appear to be along this line, but rather perpendicular to this in a primarily north-south direction.

Similar to the W 43A outflow, precession is indicated for IRAS 16342–3814, but not as a result of the available H₂O maser data. Instead, it was the Keck adaptive optics images in the near-infrared (Sahai et al. 2005) that showed a corkscrew structure inscribed on the walls of the observed lobes. The combined radio/infrared observations demonstrate that both bow shock morphologies and precession can take place in the same object. Since no such high-resolution optical/infrared imaging is available for OH 12.8–0.9 it is unknown whether precession occurs in the object, however, it is clearly not suggested by the structure or kinematics of the H₂O masers.

4. CONCLUSIONS

Using the VLBA we have shown that, like the spatial morphology, the kinematics of the H₂O masers toward OH 12.8–0.9 indicate that the object is a member of the rare “water fountain” class of sources. We find that the masers continue to be located in two distinct regions at the ends of a bipolar jet-like structure having a north-south orientation on the sky. The masers in the two regions are distributed along arc-like structures ~ 12 – 20 mas across oriented roughly perpendicular to the separation axis. The angular separation of the two regions is roughly 110 mas, with the blue-shifted masers located to the north and the red-shifted masers to the south. The arc-like arrangements of the masers are suggestive of bow shocks formed by a collimated axisymmetric wind impinging on the ambient medium surrounding the star.

The two additional epochs of VLBA observations, beyond our first epoch in 2004, have allowed us to track the projected spatial motions of individual features over the course of ~ 600 days. We find that the two maser regions maintain their arc-like appearance as they expand away from each other along the axis of separation. The observed proper motion of the southern masers relative to the northern masers is 2.76 mas yr^{-1} ($\sim 105 \text{ km s}^{-1}$ at the assumed distance of 8 kpc). The masers maintain collimation during this expansion with little motion perpendicular to the north–south axis. Combining the proper motions with the measured radial velocities yields a three-dimensional (3-D) expansion velocity of 58 km s^{-1} relative to the dynamical center of the distribution. The inclination angle of the jet is estimated to be $\sim 24^\circ$. A simple linear fit to the historical radial velocity data combined with our own measurements yields an estimate for the 3-D acceleration of $\sim 0.63 \text{ km s}^{-1} \text{ yr}^{-1}$ and a corresponding dynamical age for the outflow of $\sim 90 \text{ yr}$. Long-term VLBA monitoring of the H_2O masers should enable the determination of the tangential acceleration of the masers and the true 3-D acceleration of the outflow associated with OH 12.8–0.9.

This research has made use of the SIMBAD database, operated at CDS, Strasbourg, France. This research has made use of NASA’s Astrophysics Data System Bibliographic Services.

REFERENCES

- Aaquist, O. B. & Kwok, S. 1996, *ApJ*, 462, 813
- Baud, B., Habing, H. J., Matthews, H. E. & Winnberg, A. 1979, *A&AS*, 36, 193
- Baud, B., Sargent, A. J., Werner, M. W. & Bentley, A. F. 1985, *ApJ*, 292, 628
- Bloemhof, E.E., Reid, M.J., & Moran, J.M. 1992, *ApJ*, 397, 500
- Boboltz, D. A. and Marvel, K. B. 2005, *ApJ*, 627, 45
- Boboltz, D. A., Diamond, P. J. & Kemball, A. J. 1997, *ApJ*, 487, L147
- Chapman, J.M., Cohen, R.J., & Saika, D.J. 1991, *MNRAS*, 249, 227
- Chen, X., Shen, Z.-Q., Imai, H., & Kamohara, R. 2006, *ApJ*, 640, 982
- Claussen, M., Sahai, R., & Morris, M. 2004, *ASP Conf. Ser.* 313: *Asymmetrical Planetary Nebulae III: Winds, Structure and the Thunderbird*, 313, 331
- Condon, J.J. 1997, *PASP*, 109, 166
- Engels, D. 2002, *A&A*, 388, 252
- Engels, D., Schmid-Burgk, J. & Walmsley, C. M. 1986, *A&A*, 167, 129
- Gómez, Y., Rodríguez, L. F., Contreras, M. E. & Moran, J. M. 1994, *Revista Mexicana de Astronomia y Astrofisica*, 28, 97
- Hodge, T. M., Kraemer, K. E., Price, S. D., & Walker, H. J. 2004, *ApJS*, 151, 299
- Imai, H., Morris, M., Sahai, R. Hachisuka, K. & Azzolini F, J. R. 2004, *A&A*, 420, 265
- Imai, H., Nakashima, J.-i., Diamond, P. J., Miyazaki, A., & Deguchi, S. 2005, *ApJ*, 622, L125
- Imai, H., Obara, K., Diamond, P. J., Omodaka, T. & Sasao, T. 2002, *Nature*, 417, 829
- Kemball, A.J. 1992, Ph.D. Thesis, Rhodes Univ.
- Kwok, S. 1993, *ARA&A*, 31, 63
- Kwok, S., Volk, K. & Bidelman, W. P. 1997, *ApJS*, 112, 557
- Likkell, L., Morris, M. & Maddalena, R. J. 1992, *A&A*, 256, 581

- Manchado, A., Villaver, E., Stanghellini, L., & Guerrero, M. A. 2000, ASP Conf. Ser. 199: Asymmetrical Planetary Nebulae II: From Origins to Microstructures, 199, 17
- Marvel, K.B. 1996, Ph.D. Thesis, New Mexico State Univ.
- Morris, M. R., Sahai, R. & Claussen, M. 2003, RevMexAA, 15, 20
- Sahai, R., Te Lintel Hekkert, P., Morris, M., Zijlstra, A., & Likkell, L. 1999, ApJ, 514, L115
- Sahai, R. & Trauger, J. T. 1998, AJ, 116, 1357
- Sahai, R., Le Mignant, D., Sánchez Contreras, C., Campbell, R. D., & Chaffee, F. H. 2005, ApJ, 622, L53
- te Lintel Hekkert, P., Versteeg-Hensel, H. A., Habing, H. J. & Wiertz, M. 1989, A&AS, 78, 399

Table 1. H₂O maser characteristics derived from the epoch 1 (2004 June 21) VLBA data.

v_{LSR} (km s ⁻¹)	S_ν (Jy beam ⁻¹)	σ_{S_ν} (Jy beam ⁻¹)	Relative R.A. (mas)	$\sigma_{\text{R.A.}}$ (mas)	Relative Dec. (mas)	$\sigma_{\text{Dec.}}$ (mas)
Blue-shifted masers						
-85.07	0.044	0.009	5.869	0.038	2.520	0.063
-83.32	0.052	0.009	14.806	0.034	-10.133	0.049
-81.71	1.297	0.012	0.000	0.006	0.000	0.008
-81.67	0.123	0.012	-1.813	0.031	-0.322	0.045
-80.88	0.261	0.009	7.647	0.009	0.376	0.014
Red-shifted masers						
-34.61	0.247	0.009	1.116	0.012	-108.821	0.019
-33.92	0.139	0.012	-5.773	0.018	-108.460	0.027
-33.72	0.498	0.012	2.235	0.018	-108.856	0.030
-33.27	1.041	0.012	-2.807	0.005	-108.597	0.007
-32.58	0.499	0.009	5.297	0.010	-106.906	0.017

Table 2. H₂O maser characteristics derived from the epoch 2 (2005 Nov. 2) VLBA data.

v_{LSR} (km s ⁻¹)	S_ν (Jy beam ⁻¹)	σ_{S_ν} (Jy beam ⁻¹)	Relative R.A. (mas)	$\sigma_{\text{R.A.}}$ (mas)	Relative Dec. (mas)	$\sigma_{\text{Dec.}}$ (mas)
Blue-shifted masers						
-83.29	0.153	0.009	15.458	0.029	-10.516	0.045
-81.57	1.323	0.010	0.000	0.017	0.000	0.028
-81.41	0.096	0.010	-2.207	0.041	-0.456	0.063
-80.73	0.216	0.010	8.174	0.032	0.173	0.051
Red-shifted masers						
-34.47	0.468	0.010	1.286	0.020	-112.898	0.033
-33.54	0.293	0.009	2.518	0.020	-112.793	0.034
-33.31	0.086	0.009	-6.432	0.048	-112.695	0.071
-33.10	0.569	0.009	-2.658	0.020	-112.669	0.030
-32.68	0.142	0.009	5.765	0.034	-110.732	0.051

Table 3. H₂O maser characteristics derived from the epoch 3 (2006 Feb. 24) VLBA data.

v_{LSR} (km s ⁻¹)	S_ν (Jy beam ⁻¹)	σ_{S_ν} (Jy beam ⁻¹)	Relative R.A. (mas)	$\sigma_{\text{R.A.}}$ (mas)	Relative Dec. (mas)	$\sigma_{\text{Dec.}}$ (mas)
Blue-shifted masers						
-83.29	0.174	0.013	15.580	0.029	-10.741	0.054
-81.54	0.970	0.013	0.000	0.026	0.000	0.043
-81.30	0.079	0.013	-2.358	0.063	-0.384	0.110
-81.26	0.065	0.013	0.347	0.068	1.034	0.111
-80.72	0.094	0.012	8.208	0.043	0.067	0.074
Red-shifted masers						
-34.44	0.228	0.015	1.315	0.039	-113.770	0.072
-33.46	0.151	0.014	2.582	0.039	-113.587	0.070
-33.35	0.061	0.012	-6.378	0.062	-113.447	0.106
-33.04	0.164	0.012	-2.593	0.041	-113.582	0.075
-32.71	0.123	0.012	5.717	0.047	-111.546	0.085

Table 4. Velocity separation of blue- and red-shifted water masers.

Obs. Date (yr)	Δv (km s ⁻¹)	$\sigma_{\Delta v}$ (km s ⁻¹)	Spectral res. (km s ⁻¹)	Ref.
1987.452	38.8	1.5	0.16	1
1988.516	37.7	1.6	0.16	1
1990.132	42.0	2.1	0.16	1
1990.249	41.2	2.3	0.16	1
1991.332	41.5	2.1	0.16	1
1992.049	42.0	2.0	0.16	1
1992.975	42.3	2.3	0.16	1
1994.184	40.9	2.1	0.16	1
1995.186	42.4	2.0	0.16	1
1996.675	43.3	2.3	0.16	1
1999.088	44.6	2.0	0.16	1
2004.473	48.7	1.6	0.22	2
2005.838	48.3	1.3	0.22	2
2006.151	48.2	1.3	0.22	2

Note. — References: (1) Engels (2002), (2) this work.

Table 5. Summary of the H₂O maser characteristics for the water fountain sources.

Characteristic	OH 12.8–0.9	W 43A	IRAS 19134+2131	IRAS 16342–3814
Distance (kpc)	8	2.6	16	2
S _{peak} (Jy) ^a	1.4–13.0	11.5–56.6	1.2–6.0	16.0–67.7
Angular Extent (mas) ^b ..	110	920	135	3000
Linear Extent (AU) ^b	880	2400	2180	6000
Outflow Collimation (deg.)	15	5	10	6
Inclination Angle (deg.) ^c	24	39	25	40 ^d
Outflow Velocity:				
<i>v</i> _{tan} (km s ⁻¹)	53	110	120	...
<i>v</i> _{rad} (km s ⁻¹)	24	90	65	130
<i>v</i> _{tot} (km s ⁻¹)	58	145	130	...
Outflow Acceleration:				
<i>a</i> _{rad} (km s ⁻¹ yr ⁻¹)	0.53
Dynamical Age (yr)	90	50	50	150 ^d
References	1, 2, 3	4, 5, 6	4, 7	4, 8, 9, 10

^aRange over multiple epochs of single dish observations.

^bMeasured in the plane of the sky.

^cRelative to the plane of the sky.

^dFrom OH maser observations.

Note. — References: (1) Engels (2002), (2) Boboltz & Marvel (2005), (3) this work, (4) Likkell et al. (1992), (5) Imai et al. (2002), (6) Imai et al. (2005), (7) Imai et al. (2004), (8) Sahai et al. (1999), (9) Morris et al. (2003), (10) Claussen et al. (2004).

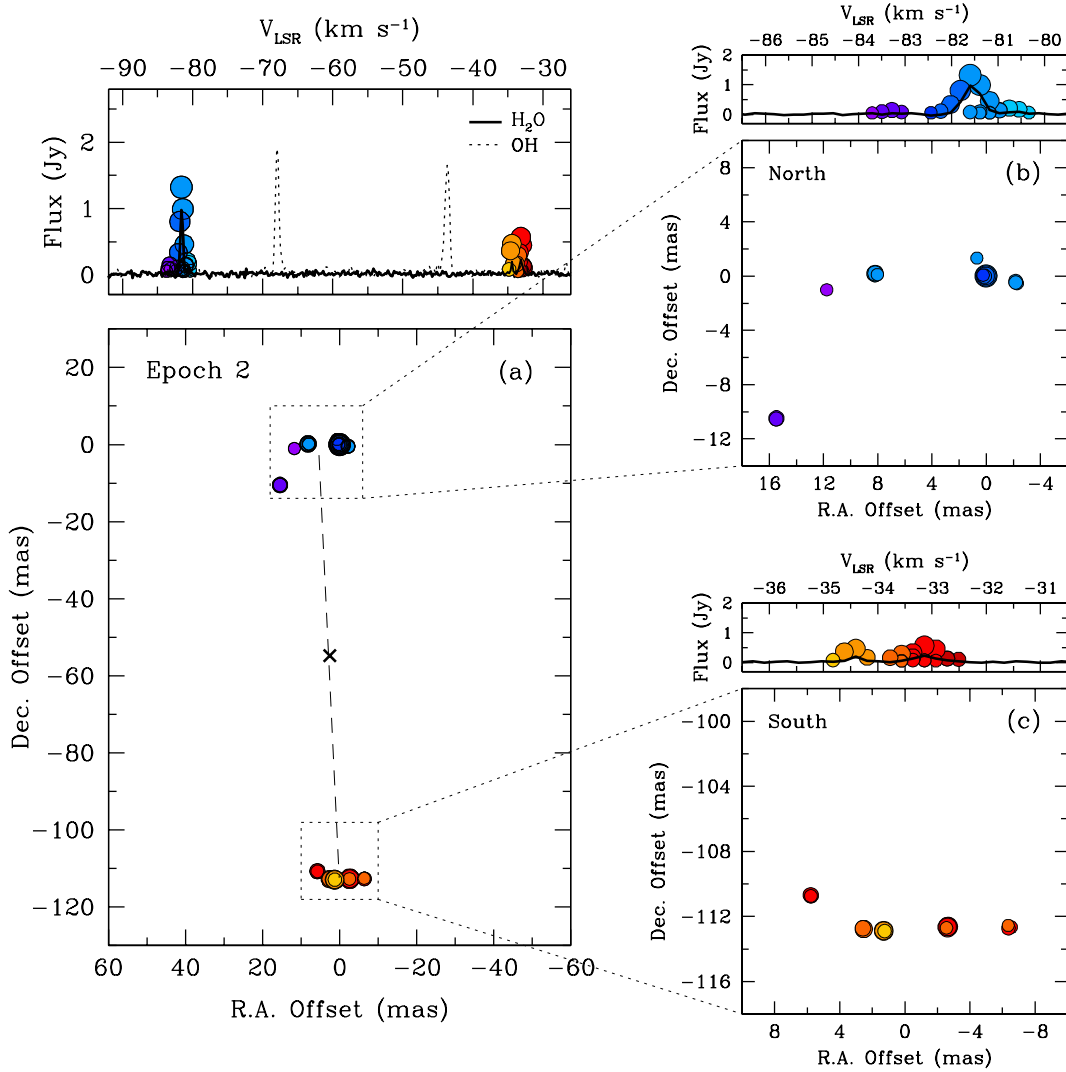


Fig. 1.— The H₂O maser emission toward OH 12.8–0.9 from epoch 2 (2005 Nov. 2). In panels (a), (b) and (c), the top sub-panels show the spectra formed by plotting maser component flux density versus LSR velocity, color-coded according to maser velocity. A dark solid line in each upper sub-panel represents the scalar-averaged cross-power spectrum on the Los Alamos–Pie Town VLBA baseline. A dotted line in the top sub-panel of (a) represents the scalar-averaged cross-power spectrum of the OH masers (with the flux density scaled by a factor of 0.5) from the Los Alamos–Pie Town baseline. The lower sub-panels in (a), (b) and (c) plot the spatial distribution of the H₂O masers with point-color representing the corresponding velocity bin in the spectrum and point-size proportional to the logarithm of the maser flux density. Panel (a) shows all H₂O maser components from our VLBA observations. A dashed line represents the axis of separation between the centers of the blue- and red-shifted masers at a position angle of 2.6° east of north. The “x” symbol represents the midpoint of the bipolar distribution. Panels (b) and (c) show expanded views of the blue- and red-shifted maser features respectively. Errors in the positions of the features are smaller than the data points for all panels.

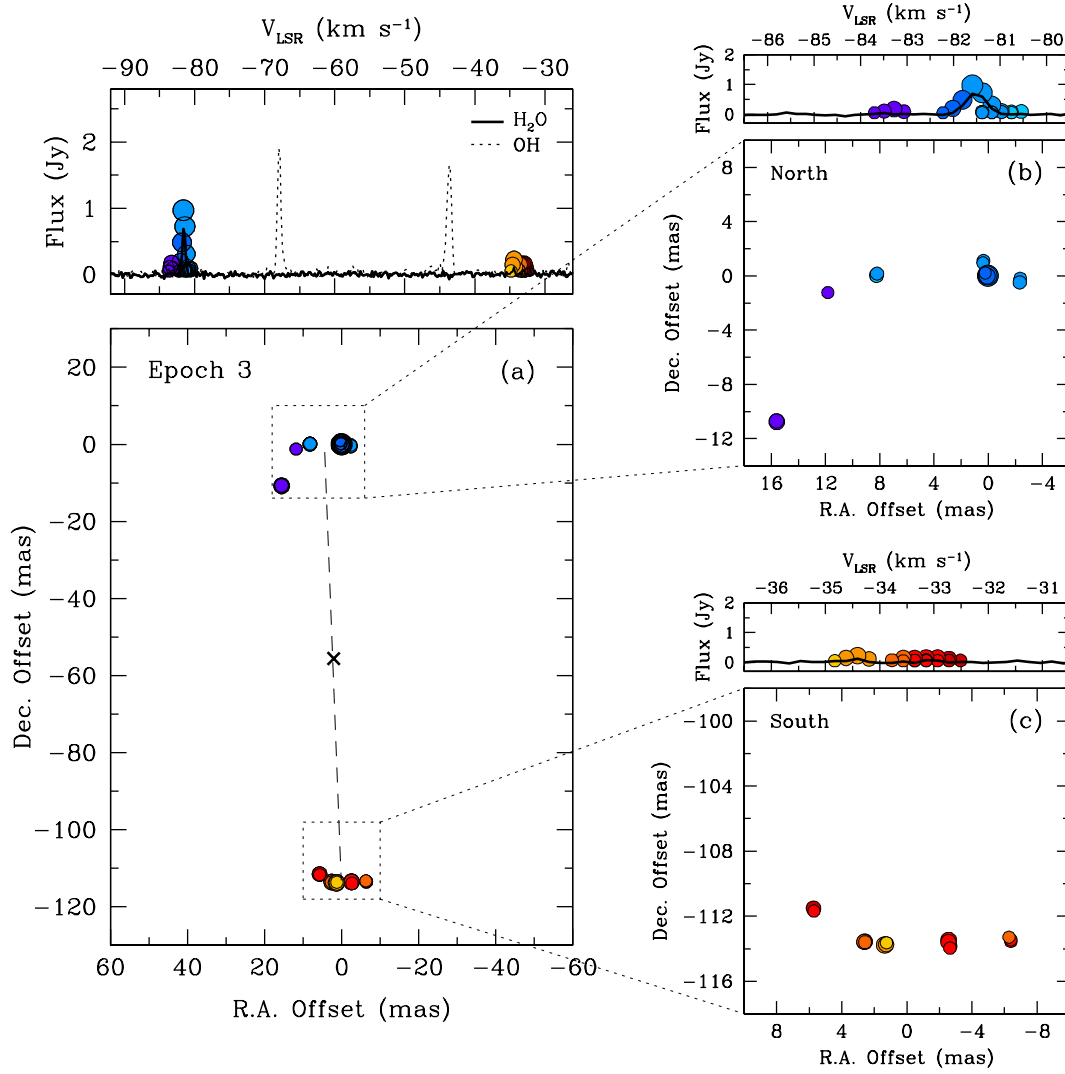


Fig. 2.— Same as Figure 1, but for epoch 3 (2006 Feb. 24).

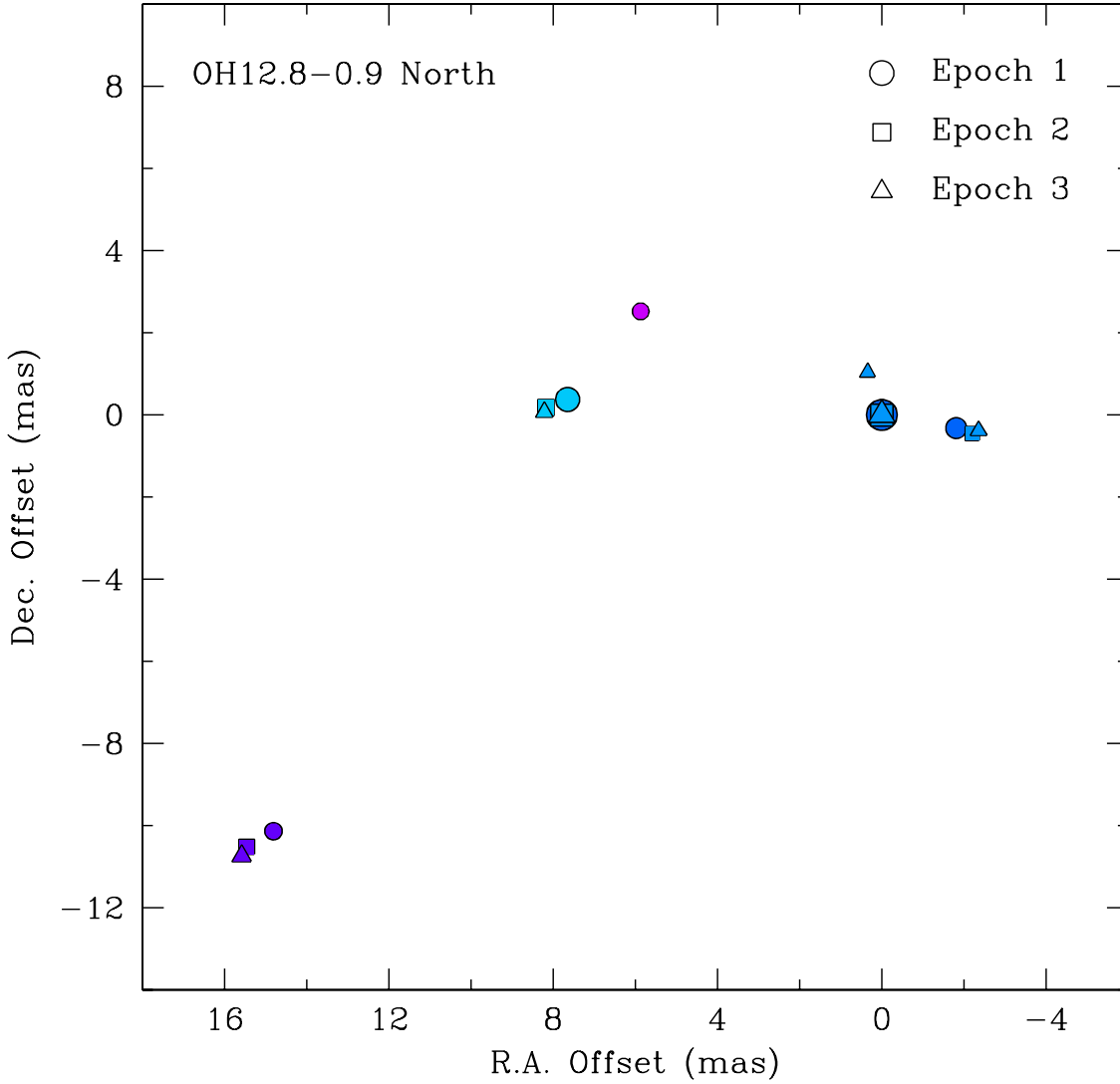


Fig. 3.— Northern blue-shifted masers associated with OH12.8–0.9 for all three epochs (2004 June 21, 2005 Nov. 2, and 2006 Feb. 24). Masers are color-coded according to velocity and point-size is proportional to the logarithm of the maser flux density. There are four maser features common to all three epochs including the reference feature at (0,0). The masers show little motion relative to this stationary reference feature.

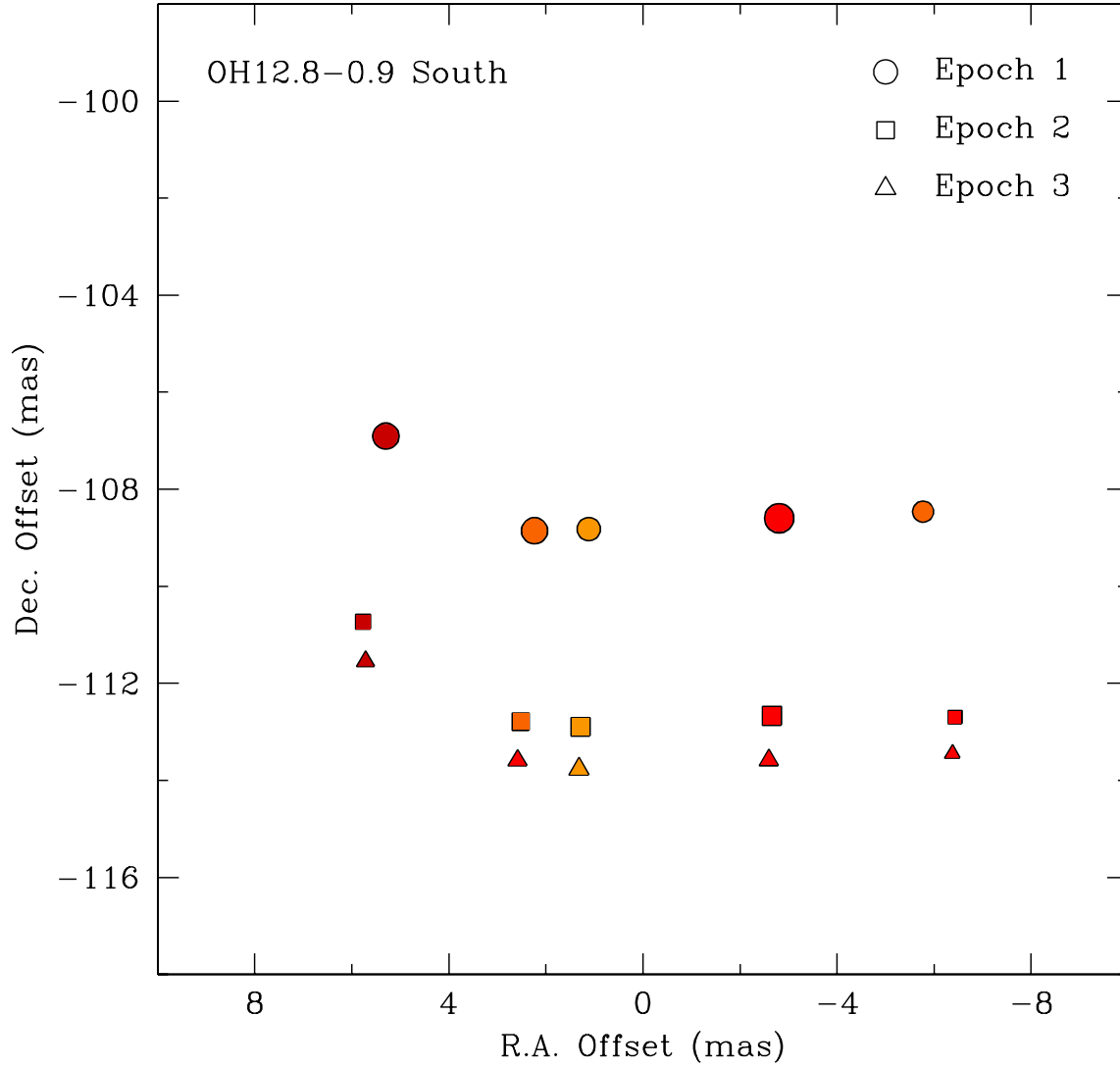


Fig. 4.— Southern red-shifted masers associated with OH 12.8–0.9 for all three epochs (2004 June 21, 2005 Nov. 2, and 2006 Feb. 24) demonstrating the motions of the masers over time relative to the reference feature in Figure 3. Masers are again color-coded according to velocity and point-size is proportional to the logarithm of the maser flux density. All five features are common to all three epochs.

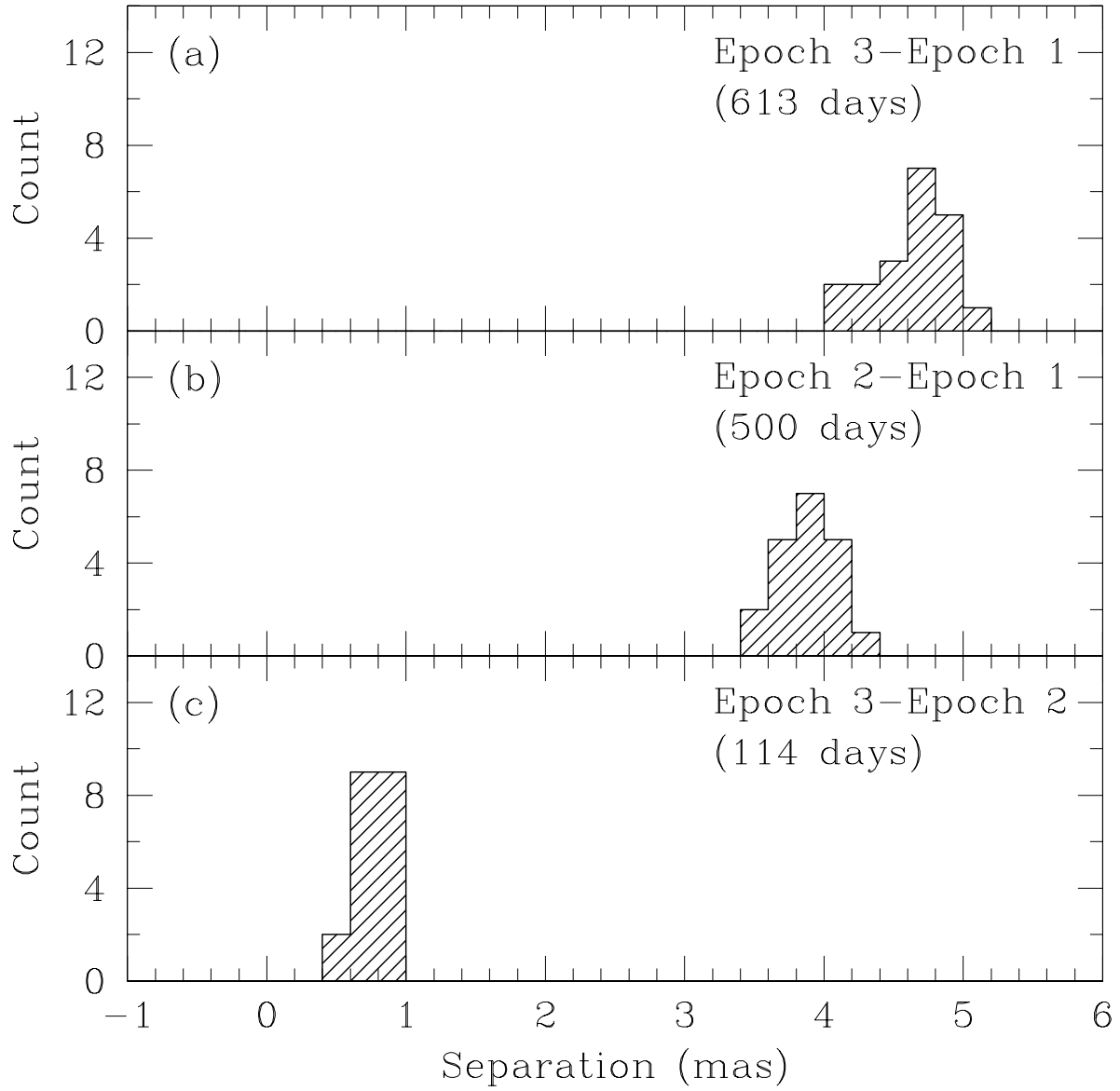


Fig. 5.— Histogram showing the pairwise spatial separations between combinations of northern and southern maser pairs for (a) epochs 3 and 1, (b) epochs 2 and 1, and c) epochs 3 and 2. Listed in each panel is the elapsed time between epochs in days.

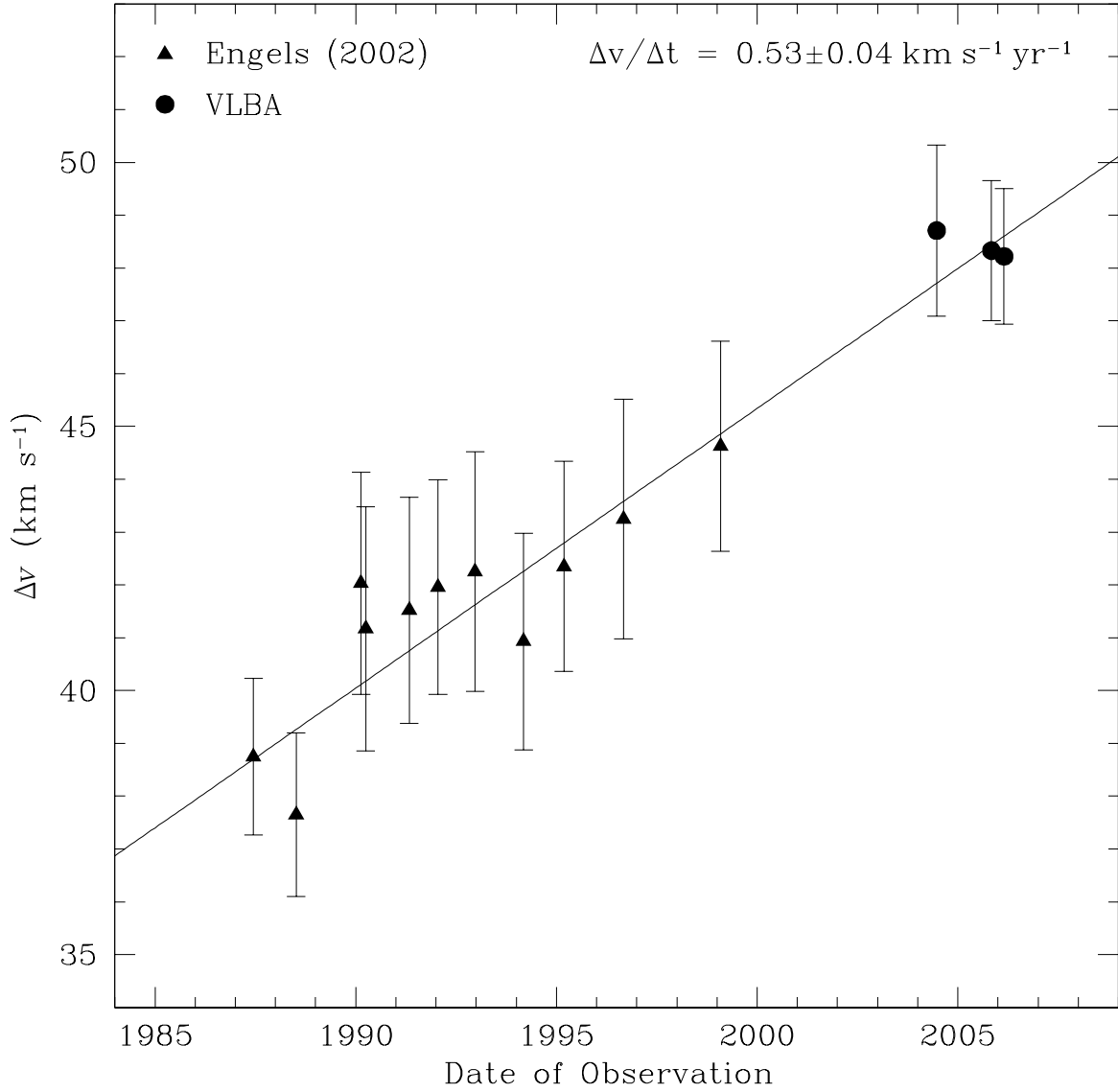


Fig. 6.— Plot showing the measured velocity separation (Δv) of the blue- and red-shifted water maser features as a function of time from values listed in Table 4. The line represents a weighted linear least-squares fit to the data and indicates a constant acceleration of $0.53 \text{ km s}^{-1} \text{ yr}^{-1}$.